The Visualization of Myocardial Strain for the Improved Analysis of Cardiac Mechanics

Burkhard C. Wünsche* and Richard Lobb†
Division for Biomedical Imaging and Visualization, Department of Computer Science
University of Auckland, Auckland, New Zealand
Alistair A. Young‡
Department of Anatomy with Radiology, Department of Physiology
University of Auckland, Auckland, New Zealand

Abstract

Heart diseases cause considerable morbidity and the prognosis after heart failure is poor. An improved understanding of cardiac mechanics is necessary to advance the diagnosis and treatment of heart diseases. This paper presents techniques for visualizing and evaluating biomedical finite element models and demonstrates their application by using as an example models of a healthy and a diseased human left ventricle. The following contributions are made: we apply techniques traditionally used in solid mechanics and computational fluid dynamics to biomedical data and suggest some improvements and modifications. We introduce a novel algorithm for computing isosurfaces for scalar fields defined over curvilinear finite elements. We obtain new insight into the mechanics of the healthy and the diseased left ventricle and we facilitate the understanding of the complex deformation of the heart muscle by novel visualizations.

CR Categories: I.3.8 [Computer Graphics]: Applications; I.3.6 [Computer Graphics]: Methodology and Techniques—Graphics Data Structures and data types; I.3.3 [Computer Graphics]: Picture/Image Generation; I.6.5 [Simulation and Modeling]: Model Development—Modeling methodologies; J.3 [Computer Applications]: Life and Medical Sciences

Keywords: visualization, isosurfaces, tensor fields, finite elements, myocardial deformation, myocardial strain

1 Introduction

Heart diseases remain the biggest killer in the western world [Masood et al. 2000]. Heart diseases can result in heart failure, which is a clinical syndrome that arises when the heart is unable to pump sufficient blood to meet the metabolic needs of the body at normal filling pressures [Alexander et al. 1994]. The acquisition and vi-

*e-mail: burkhard@cs.auckland.ac.nz
†e-mail: richard@cs.auckland.ac.nz
‡e-mail: a.young@auckland.ac.nz

sualization of cardiac imaging data improves the diagnosis and the understanding of the development and progress of heart diseases.

The cardiac data set used in this work is a finite element model of the human left ventricle developed by Young et al. [Young et al. 1994b; Young et al. 1994a]. The deformation of the *myocardium* (heart muscle) is represented by the *strain tensor*. We use a visualization toolkit specifically designed for biomedical models [Wünsche 2003b; Wünsche 2003a] to visualize the strain tensor field and to evaluate the performance of a healthy and a diseased human left ventricle.

After introducing the left-ventricular model we visualize left-ventricular deformation by applying visualization techniques from computational fluid dynamics (CFD) and structural engineering to the biomedical field. We suggest several modifications and improvements, present a new method for computing topologically correct isosurfaces from scalar fields defined over curvilinear finite element domains, and we explain the interpretation of the visualizations. We conclude with a discussion of our results and mention avenues for future research.

2 Finite Element Modeling of the Left Ventricle

As shown in figure 1 (a) the heart consists of two main chambers, the left and the right ventricle. When discussing the heart it is convenient to introduce names for the different regions of the *myocardium* (heart muscle) as illustrated in part (b) the figure. Note that the myocardium is divided into a *subepicardial*, *subendocardial*, and a *midmyocardial* region. The terms refer to the parts of the myocardium neighboring the *epicardial surface* (the outer layer of the heart muscle), the *endocardial surface* (the layer lining the ventricular cavity), and the region between them, respectively.

The contraction of the heart is called *systole* and the expansion *diastole*. The moment of maximum contraction of the left ventricle is called (left-ventricular) *end-systole* and the moment of maximum expansion is called (left-ventricular) *end-diastole*.

2.1 Finite-Element Geometry

The geometry of a *finite element* (FE) model is described by a set of nodes and a set of elements, which have these nodes as vertices. The nodal coordinates are interpolated over an element using *interpolation functions*. Curvilinear elements can be defined by specifying nodal derivatives.

As an example of a finite element consider the cubic Hermite-linear Lagrange element in two dimensions shown in figure 2. We first specify a parent element, shown in part (a) of the figure, which is a square in the ξ-parameter space (*material space*). The coordinates ξ_i ($0 \leq \xi_1, \xi_2 \leq 1$) are called the element or *material co-*
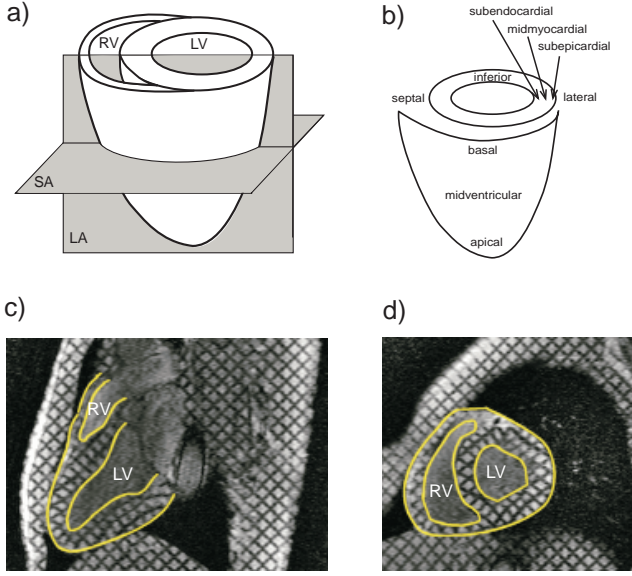
Figure 1: (a) Schematic drawing of a heart with the left (LV) and the right (RV) ventricle being indicated. (b) Illustration of the regions of the left-ventricular myocardium. (c,d) Long axis (LA) and short axis (SA) tagged MRI images of a heart with the endocardial and the epicardial surface indicated in yellow.

ordinates. The value of some variable u (e.g., temperature) at the material coordinates ξ is defined by interpolating the nodal values u_i. In our example we assume that derivatives in ξ_1-direction $\left(\frac{\partial u}{\partial \xi_1}\right)_i$ $(i = 1, \ldots, 4)$ are specified at the element nodes, enabling a cubic Hermite interpolation to be performed in that direction. A linear interpolation is performed in the ξ_2-direction.
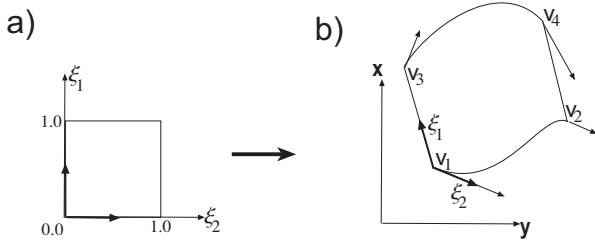

Figure 2: A cubic Hermite-linear Lagrange finite element.

The cubic Hermite-linear interpolation of u over the entire 2D parameter space is then defined by the tensor products of the interpolation functions in each parameter direction:

$$
\begin{aligned}
u(\xi_1, \xi_2) &= H_1^0(\xi_1)L_1(\xi_2)u_1 + H_2^0(\xi_1)L_1(\xi_2)u_2 \\
&+ H_1^0(\xi_1)L_2(\xi_2)u_3 + H_2^0(\xi_1)L_2(\xi_2)u_4 \\
&+ H_1^1(\xi_1)L_1(\xi_2)\left(\frac{\partial u}{\partial \xi_1}\right)_1 + H_2^1(\xi_1)L_1(\xi_2)\left(\frac{\partial u}{\partial \xi_1}\right)_2 \\
&+ H_1^1(\xi_1)L_2(\xi_2)\left(\frac{\partial u}{\partial \xi_1}\right)_3 + H_2^1(\xi_1)L_2(\xi_2)\left(\frac{\partial u}{\partial \xi_1}\right)_4
\end{aligned}
$$

where

$$
L_1(\xi) = 1 - \xi, \quad \text{and} \quad L_2(\xi) = \xi \tag{1}
$$

are the one-dimensional linear Lagrange basis functions, and

$$
\begin{aligned}
H_1^0(\xi) &= 1 - 3\xi^2 + 2\xi^3, & H_1^1(\xi) &= \xi(\xi - 1)^2 \\
H_2^0(\xi) &= \xi^2(3 - 2\xi), & H_2^1(\xi) &= \xi^2(\xi - 1)
\end{aligned} \tag{2}
$$

are the one-dimensional cubic Hermite basis functions.

The geometry of an element in world coordinates (figure 2 (b)) is obtained by specifying the world-coordinates $\mathbf{v}_i$ and the ξ_1-tangents $\left(\frac{\partial \mathbf{v}}{\partial \xi_1}\right)_i$ $(i = 1, \ldots, 4)$ of the element vertices and interpolating them as above.

2.2 The Left-Ventricular Finite Element Model

The time-varying geometry of the left-ventricular model is obtained non-invasively by tracking myocardial contours on tagged MRI slices and by fitting a surface through them as indicated in figure 4 [Young et al. 1995]. The resulting finite element model consists of 16 finite elements with its geometry being interpolated in radial direction using linear Lagrange basis functions and in the circumferential and longitudinal directions using cubic Hermite basis functions.

Model geometries were generated for the maximum expansion (end-diastole) and maximum contraction (end-systole) and are shown in figure 3.
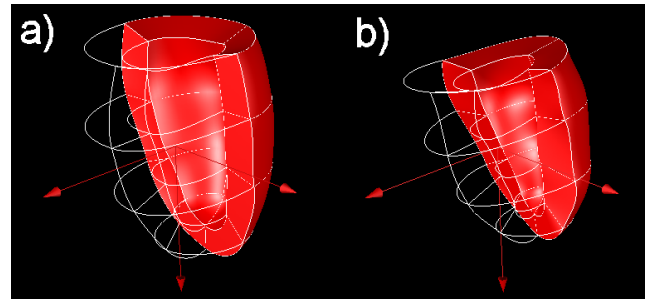

Figure 3: The finite element model of the left ventricle at end-diastole (a) and end-systole (b).

In addition the cavities of each model can be represented by finite elements which is useful for computing ventricular performance measures [Wünsche and Young 2003; Wünsche 2003a]. Examples are seen in figure 5 which shows the model of a healthy left ventricle (a) and the model of a heart diagnosed with non-ischemic *dilated cardiomyopathy* (b), which is characterized by cardiac enlargement, increased cardiac volume, reduced ejection fraction, and congestive failure [Young et al. 2000].

2.3 Myocardial Strain

Causes of heart failure are differentiated into mechanical, myocardial, and rhythmic abnormalities [Alexander et al. 1994]. Examples are increased pressure or volume load (e.g., due to a dysfunctional valve), *ischemia* (blockage of the coronary artery) and conduction disturbances including standstill and irregular heart beat (*fibrillation*). The analysis of myocardial function is important for the diagnosis of heart diseases, the planning of therapy [Lim and Choi 1999] and the understanding of the effect of cardiac drugs on regional function [Reichek 1999].

Many cardiac disorders result in regionally altered myocardial mechanics. Traditionally an abnormal contractile function of the ventricles has been determined by measuring the wall thickening using cine MRI images, echocardiography and SPECT [Alexander
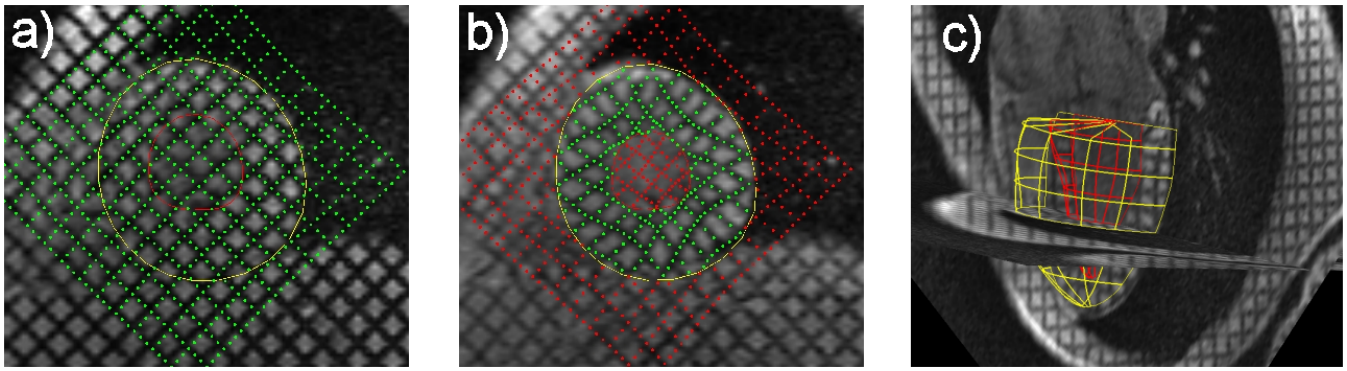
Figure 4: Tag lines before (a) and after (b) myocardial contraction and the fitted epicardial and endocardial surface (c).
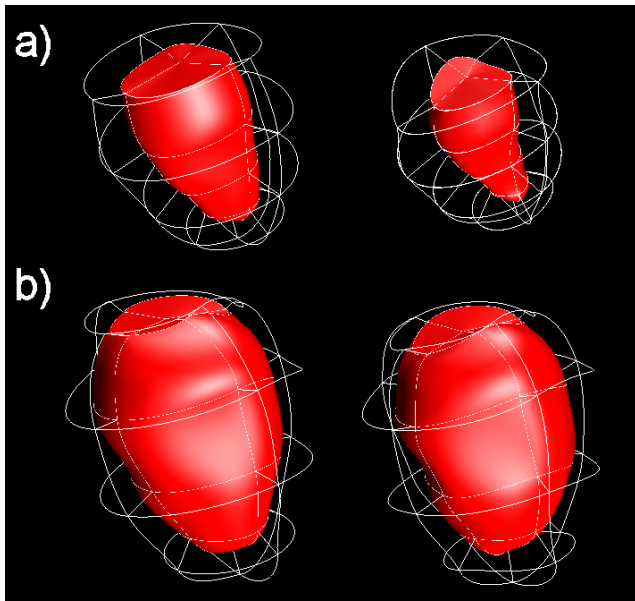
et al. 1994]. Wall thickening, however, is only one indicator of impending heart failure and other motion dependent indicators have been reported in the literature [de Simone et al. 1996; Guttman et al. 1997]. A full description of the deformation behavior of the myocardium is therefore desirable. Such a description is given by the (Lagrangian) strain tensor **E**.

Strain information is obtained from tagged MRI images as shown in figure 4. When the heart deforms the tag lines deform with it making it possible to compute the displacement field **u** [Young et al. 1994a]. The (Lagrangian) strain tensor **E** is computed from the *displacement gradient* tensor $\nabla \mathbf{u}$ using the equation

$$\mathbf{E} = \frac{1}{2}\left((\nabla \mathbf{u}) + (\nabla \mathbf{u})^T + (\nabla \mathbf{u})^T(\nabla \mathbf{u})\right) \quad (3)$$

The tensor describes the pure deformation of an infinitesimal material volume without rotation and translation. Scalar strain values can be derived from the strain tensor to quantify the length change of an infinitesimal material volume in a given direction (e.g., the circumferential or radial direction of the ventricle). Negative strain values are interpreted as a local shortening of the myocardium and positive strain values as a local elongation. The strain tensor is defined with respect to the material coordinate system, i.e., the diagonal components of the strain tensor represent the *normal strains* in the circumferential, longitudinal and radial directions, respectively. The computation of the strain field was validated using a gel phantom [Young et al. 1995].

Since the strain tensor **E** is symmetric there always exist 3 *eigenvalues* λ_i and 3 mutually perpendicular *eigenvectors* $\mathbf{v}_i$ such that [Lai et al. 1986]

$$\mathbf{E}\mathbf{v}_i = \lambda_i \mathbf{v}_i \quad i = 1, 2, 3 \quad (4)$$

The eigenvectors $\mathbf{v}_1$, $\mathbf{v}_2$, and $\mathbf{v}_3$ of **E** are the *principal directions* of the strain, i.e., the directions in which there is no shear strain. The eigenvalues λ_1, λ_2, and λ_3 are the *principal strains* and give the unit elongations in the principal directions. The maximum, medium, and minimum eigenvalue are called the *maximum, medium, and minimum principal strain*, respectively.

Abnormalities in the myocardial strain are detectable before first symptoms of a heart attack occur [Guttman et al. 1997] so that measuring and visualizing the strain might represent a useful diagnosis tool. McCulloch and Mazhari [McCulloch and Mazhari 2001] suggest several possible roles of strain and stress measurement in clinical diagnosis.

Figure 5: Ventricular cavity of the healthy heart (a) and the sick heart (b) at end-diastole (left) and end-systole (right).

3 The Visualization of Myocardial Strain

Using the finite element models in figure 5 it is possible to compute the *end-diastolic volume* (volume of blood at maximum expansion)

and the *stroke volume* (volume of blood ejected during contraction) for the healthy and the diseased heart [Wünsche and Young 2003; Wünsche 2003a]. For the diseased heart a considerable larger end-diastolic volume is observed. However, the stroke volume is only $36.23cm^3$ and about 30% smaller than for the healthy heart. These values indicate a severe impairment of myocardial function.

In order to better understand the local deformation of the myocardium more information is required. This section presents and explains various visualizations of the strain tensor and of quantities derived from it. Most visualization methods in this section visualize the strain tensor by using its principal directions and principal strains explained in subsection 2.3.

3.1 Color Mapping

A popular method for visualizing scalar fields over 2D domains is color mapping which associates a range of scalar field values with a color spectrum. The domain of the scalar field in then rendered in the appropriate colors.

Our visualization toolkit contains a global list of color maps which can be used for multiple icons of the same or different models. In order to minimize artifacts due to color interpolation the color maps are implemented using a one-dimensional texture map. This enables us to create *color map markers* [Wünsche 2003b]. Markers are inserted into the color spectrum at user defined field values and appear as isocontours on a color mapped surface as illustrated in figure 6 (a). The image visualizes the strain in the radial direction on the endocardial surface. The marker represents the 0-isocontour and it can be seen that the subendocardial wall thickens almost everywhere.
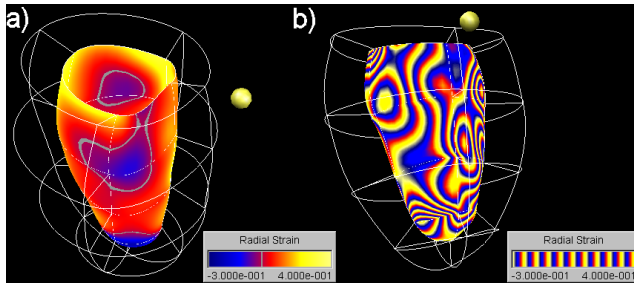

Figure 6: The radial strain field on the endocardial surface visualized using a color map with a color marker indicating zero strain values (a) and a cyclical color map (b). The septal wall is indicated by a yellow sphere.

Additional information can be revealed by using cyclical color maps which map several cycles of a color spectrum over the specified field range. We have found cyclical color maps are especially useful for displaying the fine structure of a scalar field and to uncover symmetries and discontinuities [Wünsche 2003a]. Figure 6 (b) shows clearly C^1-discontinuities in the radial strain field across some element boundaries which are not visible in (a). After discussing this observation with the developers of the heart model we found that the technique used for fitting the strain field to the finite elements guarantees only C^0-continuity.

Also note that the contour density and contour normal direction of the resulting surface texture indicate the magnitude and direction, respectively, of the visualized scalar field.

3.2 Displacement Field Visualization

The movement of the heart during contraction can be studied by visualizing the displacement field between end-diastole and end-systole. Figure 7 (a) indicates the displacement at selected material points with red arrows. It can be seen that the heart moves during contraction towards the apex.

In order to analyze rotational movements we project the displacement vectors onto a radial-circumferential material plane. The results visualized in figure 7 (b) illustrate that the apex rotates overall anticlockwise (apex-to-base view) whereas the base moves in the radial direction.
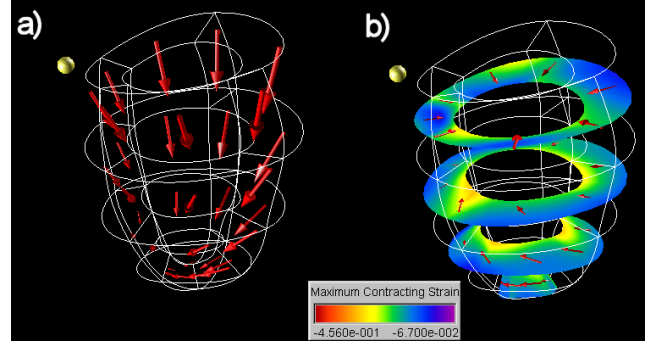

Figure 7: The displacement field of the contracting left ventricle visualized using vector arrows (a) and vector arrows projected onto a radial-circumferential material plane (b).

3.3 Tensor Ellipsoids

Figure 8 shows tensor ellipsoids which visualize the full tensor information at regular sample points throughout the midmyocardium. Tensor ellipsoids encode the principal directions and strains by the directions and lengths, respectively, of the axes of the ellipsoid. In order to encode the sign of an eigenvalue we divide an ellipsoid into six segments using a hexagonal subdivision of the unit sphere (see insert of figure 8). A red segment indicates expansion and a blue segment indicates contraction. Ellipsoids are formed by scaling the unit sphere with the eigenvalues of the visualized tensor and by rotating it using a coordinate transformation matrix which has the corresponding normalized eigenvectors as columns.

Note that the 3D geometry is difficult to perceive from a static image. Rotating the model enables the brain to differentiate ellipsoids in the foreground and background. Consequently our toolkit incorporates a function to animate the trackball which is used to rotate the model.
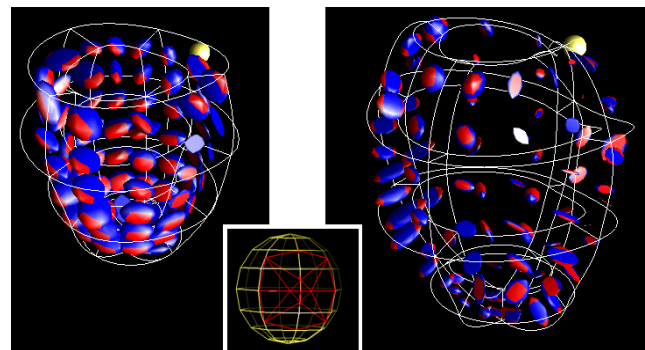

Figure 8: The strain field in the mid-wall of the healthy (left) and diseased (right) left ventricle visualized using tensor ellipsoids. The septal wall is indicated by a yellow sphere.

Figure 8 shows that for the healthy ventricle the myocardium expands in the radial direction (wall thickening) and contracts in the longitudinal and circumferential direction with the circumferential contraction being in general larger. The contraction is smallest in the septum and largest in the free wall. The results correspond well with measurements reported in the literature [Young et al. 1994a; Guttman et al. 1997].

The deformation of the sick ventricle is highly abnormal. Whereas the anterior-lateral wall of the ventricle displays an almost normal deformation behavior, albeit with smaller strain values, the situation is the exact opposite in the septal wall of the ventricle. Here the myocardium is contracting in the radial direction and is expanding in the circumferential and longitudinal direction.

3.4 Streamlines

While tensor ellipsoids contain the complete tensor information the resulting visualizations suffer from visual cluttering. Furthermore information is only displayed at selected sample points. A continuous representation of a vector field (e.g., an eigenvector field) along a line is obtained by using *streamlines* which are at each point tangential to the underlying vector field. Mathematically a streamline can be described as an integral curve $\mathbf{x}(s)$ which satisfies

$$\frac{d\mathbf{x}}{ds} = \mathbf{v}(\mathbf{x}(s)) \,, \qquad \mathbf{x}(0) = \mathbf{x}_0 \qquad (5)$$

where $\mathbf{v}(\mathbf{x})$ is a vector field and the initial condition $\mathbf{x}(0)$ defines the starting point $\mathbf{x}_0$ of the streamline.

In general the above system of equations has no analytic solution and is solved by numerical integration. Standard techniques for streamline integration include fixed step size integrators such as the Euler, Midpoint or Runge-Kutta method. A faster computation can be achieved by adaptive step size integration [Press et al. 1992; Hairer et al. 1993]. If the step size is too large or the curvature is too high a dense sampling of the streamline might be required in order to obtain a good visual approximation of it. The sampling can be performed as a post-integration interpolation step [Stalling and Hege 1995] or by using a specialized integrator which produces an interpolation from the integration information [Hairer et al. 1993, pp.176].
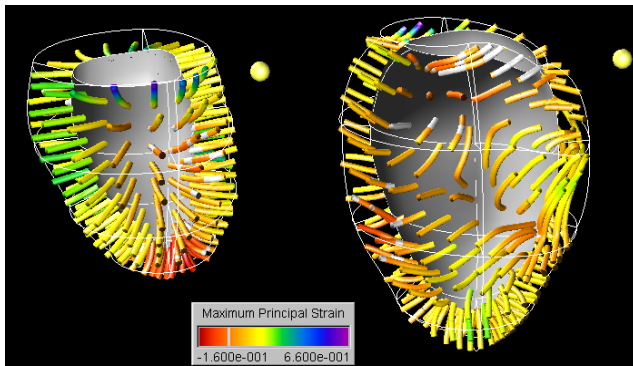

Figure 9: The strain field in the healthy (left) and the diseased (right) left ventricle visualized using streamlines in the direction of the major principal strain. The septal wall is indicated by a yellow sphere.

Figure 9 uses color mapped streamlines to visualize the direction and magnitude of the major principle strain. The gray color marker indicates zero strain values. Note that eigenvector fields are unsigned (i.e., eigenvectors have a direction but not an orientation)

and that therefore streamlines must be integrated in both the positive and the negative direction of the eigenvector field.

Streamlines are rendered as thin tubes with a constant diameter rather than as lines. Illuminating these tube-like structures gives important shape and depth cues which aid their 3D perception. We also render the endocardial wall (in gray) in order to reduce visual cluttering caused by the overlap of streamlines in the foreground and the background.

The image on the left of figure 9 shows clearly that for the healthy heart the major principal strain is oriented in the radial direction throughout the myocardial wall and that it is positive and increases toward the endocardium. This observation is consistent with an increased wall thickening towards the endocardium.

The image on the right of figure 9 confirms the previously identified abnormal contraction of the diseased left ventricle. The direction of the major principal strain is normal in the lateral wall, however, the magnitude of the major principal strain in the inferior-lateral wall is considerably smaller than for the healthy heart and is negative in some regions (indicating a wall thinning instead of a wall thickening). In the septal wall of the diseased heart the maximum principal strain is oriented in the longitudinal and the circumferential directions rather than in the radial direction.

3.5 Hyperstreamlines

Streamlines encode only one eigenvector. A continuous representation of the complete strain tensor along a line is achieved by using hyperstreamlines [Delmarcelle and Hesselink 1993].
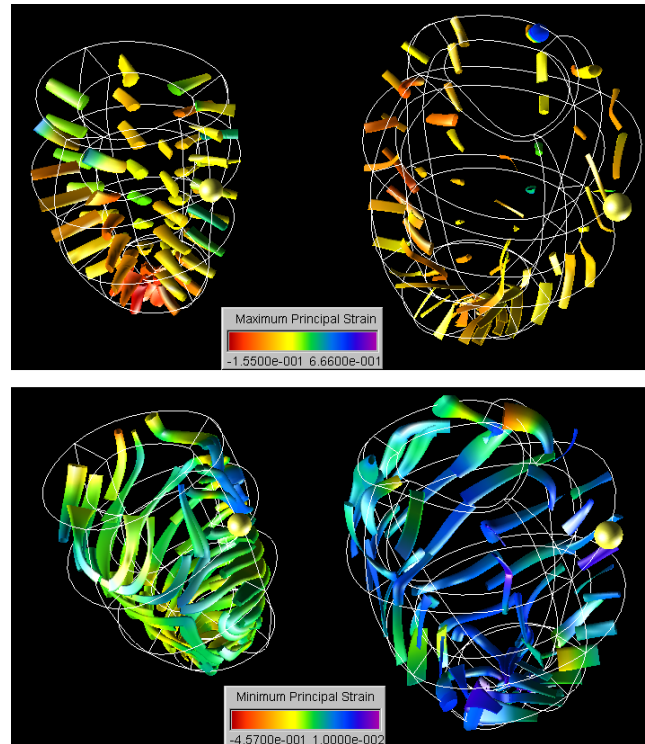

Figure 10: The strain field in the mid-wall of the healthy (left) and the diseased (right) left ventricle visualized using hyperstreamlines in the direction of the major (top) and minor (bottom) principal strain. The septal wall is indicated by a yellow sphere.

The trajectory of a hyperstreamline is a streamline in an eigenvector field as described in the previous subsection. The other two

eigenvectors and corresponding eigenvalues of the strain tensor define the axes and lengths of the ellipsoidal cross section of the hyperstreamline. The remaining eigenvalue is color mapped onto the hyperstreamline.

Figure 10 shows hyperstreamlines in the direction of the major and minor principal strain, respectively. The image on the top left of the figure shows again that for the healthy heart the major principal strain is oriented in the radial direction throughout the myocardial wall and that it is positive and increases toward the endocardium. Furthermore it can be seen from the diameter of the cross section of the hyperstreamline that with the exception of the septal wall the magnitude of the transverse strains increases from the epicardial to the endocardial surface. We are not aware of any previous work showing all these properties with a single image.

The minimum principal strain of the healthy left ventricle is compressive throughout most of the myocardium and over most of the myocardium its direction resembles a spiral moving toward the apex. This strain direction corresponds well with the motion of the heart described in the medical literature: The septum performs initially an anticlockwise rotation (apex-base view) but later a more radial movement. The apex rotates overall anticlockwise whereas the base rotates clockwise. The anterioseptal regions of the mid and apical levels and the posterioseptal region of the base perform a hook-like motion because of a reversal of rotation [Young et al. 1994a].

Note that we have in the inferior-septal region an interesting feature where the hyperstreamlines change suddenly their direction.

It is important to mention that in general the myocardium is considered incompressible. However, Denney and Prince estimate that small volume changes up to 10% occur due to myocardial perfusion [Denney, Jr. and Prince 1995]. Hence the myocardium might contain regions for which all principal strains have the same sign.

3.6 Line Integral Convolution

The above described feature where hyperstreamlines change direction can be examined in more detail using a line integral convolution texture.

Line Integral Convolution (LIC) is an effective method to visualize vector fields by using curvilinear filters to locally blur an input noise texture I along a vector field $\mathbf{v}$. The steps of the algorithm, as originally proposed by Cabral and Leedom [Cabral and Leedom 1993], are indicated in figure 11.

For any pixel $I(q,r)$ of the input texture the center $\mathbf{p}_0$ of it is used as the center of a streamline which is advected forwards and backwards by a length L. The pixels covered by the streamline are hence in forward direction

$$\mathbf{p}_i = \mathbf{p}_{i-1} + \frac{\mathbf{v}(\mathbf{p}_{i-1})}{\|\mathbf{v}(\mathbf{p}_{i-1})\|}\Delta s_{i-1}$$

where Δs_{i-1} is the distance to the pixel boundary and $s_{i+1} = s_i + \Delta s_i$. Pixels covered in backward direction are defined similarly and are indicated by negative indices. For each line segment $[s_i, s_{i+1}]$ of the streamline covering pixel p_i an exact integral of the convolution kernel $k(w)$ is computed and used as weight in the LIC

$$h_i = \int_{s_i}^{s_i+\Delta s_i} k(w)dw$$

The output pixel $O(q,r)$ is then given by

$$O(q,r) = \frac{\sum_{i=-l'}^{l} I(\mathbf{p}_i)h_i}{\sum_{i=-l'}^{l} h_i}$$

where l and l' are chosen such that the $\sum_{i=-l'}^{l} s_i = 2L$. Vector magnitude is represented either by using color mapping or by varying the length L of the filter kernel.

Parameters influencing the quality of the output texture are the input texture, the filter kernel, and the convolution length L. Most authors employ an input texture based on white noise which has a constant power spectrum and is completely random. Aliasing effects due to high frequency components in the white noise texture can be reduced by low-pass filtering the input texture [Cabral and Leedom 1993]. Stalling and Hege [Stalling and Hege 1995] suggest a modification of LIC called *Fast LIC* (FLIC) which is an order of magnitude faster, more accurate and resolution independent.

We use the direction of the minor principal strain as a vector field and use its magnitude to color map the texture. Additional details are found in [Wünsche 2003a].
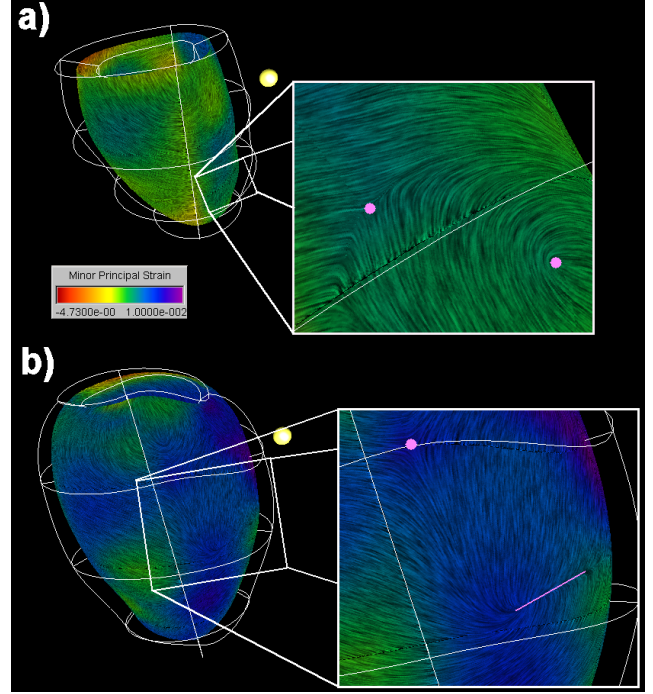

Figure 12: The minor principal strain (maximum contracting strain) of the healthy (a) and sick (b) heart visualized using Line Integral Convolution. The magenta colored points and lines indicate degenerate points.

Figure 12 (a) shows that the maximum compressive strain in the midmyocardium of the healthy heart is predominantly oriented in the circumferential direction with a slight downward tilt. Several interesting points exist where the strain suddenly changes direction. Results from tensor analysis show that these points are *degenerate points* for which at least two eigenvalues are equal [Delmarcelle and Hesselink 1994]. Two such a points are indicated by magenta colored disks in the enlarged region shown on the right hand side of the image. We found that most of the degenerate points occur on or near the septal wall. The unusual variations in strain orientation might be caused by the right ventricular wall which is connected to the left ventricular wall at both sides of the septum.

In contrast the strain field of the sick heart contains considerably more degenerate points distributed throughout the myocardium. The enlargement on the right hand side of the figure shows the presence of a line for which each point on it is a degenerate point.
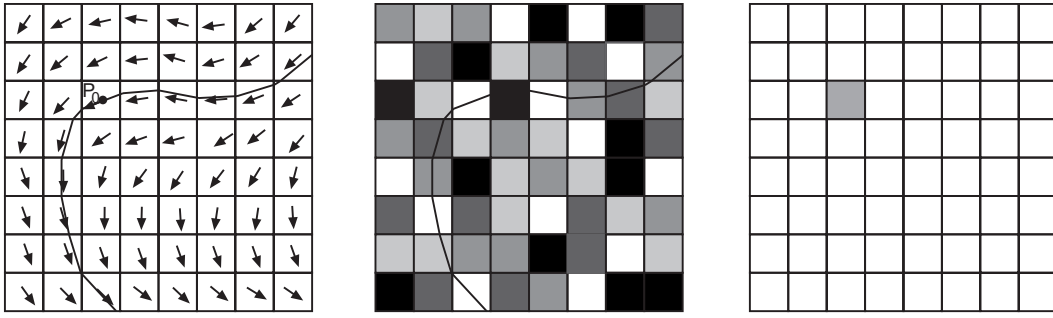
Figure 11: Vector field with a streamline through the pixel with the center p_0 (left), white noise texture (middle), and output texture of the pixel.

3.7 Isosurfaces

We have developed a polygonization algorithm which computes an isosurface in material space using a Marching Cubes type algorithm [Lorensen and Cline 1987]. The algorithm divides the cubic parent element of each (potentially curvilinear) finite element into a regular grid of $(l+1)(m+1)(n+1)$ sample values which form $l \cdot m \cdot n$ cubes in material space. The isosurface intersection with each cube is determined by considering the sign of the scalar field at the cube's vertices. Each edge with vertex values of different sign is assumed to intersect the isosurface once. The intersection point in material coordinates is approximated by linearly interpolating the scalar field values between the vertices.

In order to speed-up the isosurface computation all topologically different intersections of the isosurface with the cube are precomputed and stored in a look-up table. Since a cube has 8 vertices there are $2^8 = 256$ different configurations. Some configurations contain *ambiguous faces* for which the edge intersection points can be connected in two different ways. We create for each such configuration subcases by determining the topology of the bilinear interpolant over a face from the intersection of its asymptotes (see [Nielson and Hamann 1991; Mackerras 1992]). The result is a look-up table with 656 entries.

The surface normals of the isosurface are given by the field's gradient function if it is defined and if its use is appropriate. Otherwise the normals are determined by first precomputing the material coordinate gradients for all grid points using finite differences. For each isosurface intersection the ξ-derivative of the scalar field s at that point is then approximated by linearly interpolating the gradients at the grid vertices. Finally the surface normal is given by the gradient in world coordinates which is

$$\nabla s = \begin{pmatrix} \frac{\partial s}{\partial x_1} \\ \frac{\partial s}{\partial x_2} \\ \frac{\partial s}{\partial x_3} \end{pmatrix} = \begin{pmatrix} \sum_{i=1}^{3} \frac{\partial s}{\partial \xi_i} \frac{\partial \xi_i}{\partial x_1} \\ \sum_{i=1}^{3} \frac{\partial s}{\partial \xi_i} \frac{\partial \xi_i}{\partial x_2} \\ \sum_{i=1}^{3} \frac{\partial s}{\partial \xi_i} \frac{\partial \xi_i}{\partial x_3} \end{pmatrix} = \nabla_\xi s \, \mathbf{J}^{-1}$$

where $\mathbf{J}^{-1} = \frac{\partial \xi_i}{\partial x_j}$ is the inverse of the Jacobian of the isoparametric mapping from material to world coordinates and $\nabla_\xi s$ is the gradient of s with respect to the material coordinates.

More details are found in [Wünsche and Lin 2003].

3.7.1 Advantages

Performing the isosurface computation in material space has the advantage that scalar field values can be computed directly without performing a multi-dimensional Newton method or resampling the data. The resulting isosurface lies smoothly inside the finite ele-

ment, i.e., only very small areas of the isosurface stick out of the model boundaries and there are no erroneous results due to sample values which lie outside the model boundary and for which the scalar field is undefined. Furthermore the method is more efficient since only the actual model domain is subdivided rather than its bounding box in world coordinates. Finally the computation in material space is often more precise. For example, if tricubic elements are used then the linear interpolation used to compute the intersection points of the cube's edges with the isosurface will yield the exact result. In contrast the computation in world coordinates is exact only if the elements are cuboidal and if the sample grid is aligned with each element.
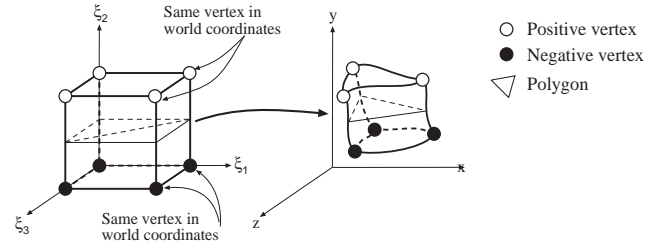

Figure 13: Isosurface within a degenerate finite element approximated with one Marching Cubes cell.

It is interesting to note that our polygonization algorithm is stable even if degenerate finite elements are used. Figure 13 gives an example of an element which has two pairs of vertices with the same world coordinates. If we approximate the finite element with a single Marching Cubes cell then we obtain two triangles (configuration 9) where one of the triangles is a line since the two edge intersections on the right face have the same world coordinates. Our algorithm removes such degenerate triangles since they do not contribute to the rendered surface and since the polygonized isosurface might be used as input to a postprocessing step such as a mesh reduction algorithm.

3.7.2 Visualization of Normal Strains

Using the above described algorithm we can compute isosurfaces to visualize the distribution of the strains in the material directions. Since the strain tensor is defined with respect to the material coordinates the strains in the circumferential, longitudinal and radial directions (the so-called *normal strains*) are given by the diagonal components E_{11}, E_{22} and E_{33}, respectively, of the strain tensor $\mathbf{E}$.

Figure 14 visualizes the normal strains on the endocardial surface using color mapping and shows additionally the 0-isosurface of each normal strain, which separates contracting and expanding regions.

The images on the left of the figure show clearly that the healthy left ventricle contracts in the circumferential and longitudinal directions and expands in the radial direction. The only exceptions are a few small regions close to the epicardial surface of the ventricle and, for the radial strain, three small cylindrical regions at the apex and the septal and lateral wall. All three normal strain components are distributed relatively evenly over the endocardial surface.

For the diseased heart the lateral wall and part of the anterior and inferior wall contract in the circumferential and longitudinal directions. Wall thickening is observed in the basal-lateral wall, the basal-septal wall and in parts of the anterior and inferior wall. The rest of the myocardium shows an abnormal deformation. As a result of the strain distribution the ventricle does not contract evenly but rather performs a shape change.

We are also interested in the shear components of the strain tensor. It is known that during contraction the heart changes predominantly in diameter. LeGrice et al. [LeGrice et al. 1995] reports 8% lateral expansion but 40% wall thickening. This indicates reorganization of the myocytes during systole. Because of the sheet structure of the myocardium it has been proposed that the sheets can slide over another restricted mainly by the length of the interconnecting collagen fibers [LeGrice et al. 1995]. The shear properties of the myocardium resulting from this sliding motion are characterized in [Dokos et al. 2002]. The shear is most restricted in the direction of the sheet normals and the maximum shear is possible in the fiber direction. Wall shear is thought to be an important mechanism of wall thickening during systole and therefore may play a substantial role in the ejection of blood from the ventricle.
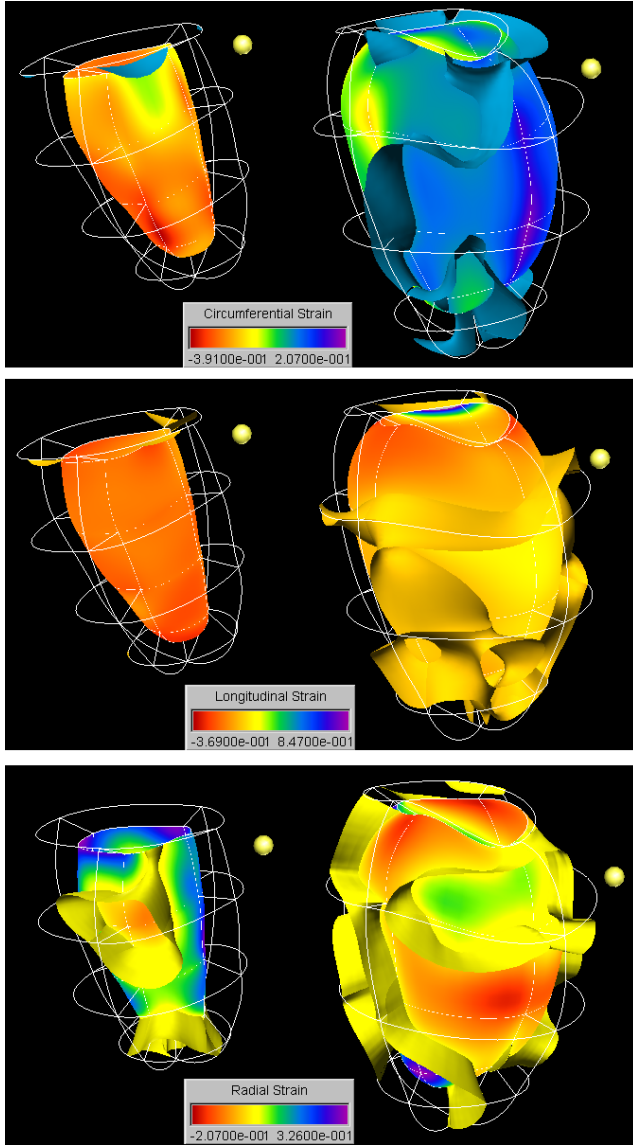

Figure 14: The normal strain in the circumferential (top), longitudinal (middle) and radial (bottom) directions on the endocardial surface of the healthy (left) and sick (right) heart. The images show also the 0-isosurface which separates regions of compressive and expanding strain. The septal wall is indicated by a yellow sphere.
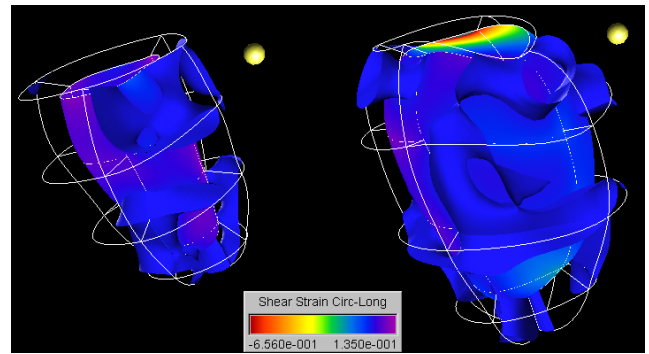

Figure 15: The circumferential-longitudinal shear strain component in the healthy (left) and sick (right) heart visualized using a color map and the 0-isosurface. The septal wall is indicated by a yellow sphere.

Figure 15 shows the shear in the circumferential-longitudinal plane. For the healthy heart the shear strain is positive for most of the myocardium with the exception of some subepicardial regions close to the merging point with the right ventricular wall. No consistent behavior can be found for the diseased heart. The shear in the lateral wall resembles most closely the normal range of values whereas the anterior-basal region exhibits extremely high negative strains, which might indicate impending tissue damage.

4 Conclusion

Visualizing the strain field improves the understanding of the complex deformation of the heart muscle. Using techniques new to the biomedical field offers additional insight.

Color maps give a good overview of the strain distribution. In order to compare two models the same color map and view parameters should be used. Spectrum markers can be used to indicate isocontours in the visualized scalar field and cyclical color maps are useful for revealing structures such as symmetries and discontinuities.

Using tensor ellipsoids, streamlines and hyperstreamlines makes it possible to visualize complex deformation behavior in a single image. Line integral convolution uncovers the presence of degenerate points at which the principal strains suddenly change direction. Further investigations are necessary to find the relationship between degenerate points, fiber structure, and the ventricular anatomy.

Isosurfaces are ideal to separate contracting and expanding regions of the heart muscle. We introduced a novel algorithm for computing isosurfaces for scalar fields defined over curvilinear finite elements. The algorithm is fast, topologically correct, gives a nearly precise fit of the isosurface with respect to the model geometry and is stable for degenerate finite elements. Ambiguous cube configurations are resolved using an efficient table look-up scheme.

Using the presented techniques we were able to visualize the myocardial strain in a healthy and a diseased left ventricle. The visualization of the healthy heart confirmed observations previously reported in the literature. Visualizing a ventricle with dilated cardiomyopathy showed that the deformation of the lateral wall resembles most closely the expected motion whereas the septal wall behaved almost contrary to the expected deformation. Very large negative shear strains were recorded in the anterior-basal wall of the ventricle. The combined effect of these deformations seems to be a pumping action by shape deformation (from circular to ellipsoidal cross section) rather then by contraction.

5 Future Research

We are interested in visualizing other data sets of diseased hearts, in particularly models of ischemic myocardium. It is known that small changes in the deformation behavior of the myocardium occur before first symptoms of a cardiac infarct develop and we hope that visualizing myocardial strain supports the detection of regions of low blood perfusion. Non-traditional visualization methods such as hyperstreamlines, LIC and tensor topology [Delmarcelle and Hesselink 1994; Lavin et al. 1997] seem to be particularly promising for this purpose.

Of special interest is the relationship between myocardial strain and fiber structure. Recent research suggests that in vivo measurement of the fiber structure is possible using diffusion tensor imaging [Sachse et al. 2001; Arts et al. 2001]. Further information could be provided by fusing our data with functional data obtained by PET and SPECT [Ruddy et al. 1999].

6 Acknowledgments

References

ALEXANDER, R. W., SCHLANT, R. C., FUSTER, V., O'ROURKE, R. A., ROBERTS, R., AND SONNENBLICK, E. H., Eds. 1994. *Hurst's The Heart*, 9th ed. McGraw-Hill Companies, Inc., London.

ARTS, T., COSTA, K. D., COVELL, J. W., AND MCCULLOCH, A. D. 2001. Relating myocardial laminar architecture to shear strain and muscle fiber orientation. *American Journal of Physiology 280*, 5 (May), H2222 – H2229. Manuscript available at URL: `http://cardiome.ucsd.edu/Publications_files/ArtSheet.pdf`.

CABRAL, B., AND LEEDOM, L. C. 1993. Imaging vector fields using line integral convolution. In *Computer Graphics (SIGGRAPH '93 Proceedings)*, Addison Wesley, J. T. Kajiya, Ed., vol. 27, ACM SIGGRAPH, 263–272.

DE SIMONE, G., DEVEREUX, R. B., KOREN, M. J., MENSAH, G. A., CASALE, P. N., AND LARAGH, J. H. 1996. Midwall left ventricular mechanics: an independent predictor of cardiovascular risk in arterial hypertension. *Circulation 93*, 2 (Feb.), 259 – 265.

DELMARCELLE, T., AND HESSELINK, L. 1993. Visualizing second-order tensor fields with hyperstreamlines. *IEEE Computer Graphics and Applications 13*, 4 (July), 25 – 33.

DELMARCELLE, T., AND HESSELINK, L. 1994. The topology of symmetric, second-order tensor fields. In *Proceedings of Visualization '94*, R. D. Bergeron and A. E. Kaufman, Eds., IEEE, 140 – 148.

DENNEY, JR., T. S., AND PRINCE, J. L. 1995. Reconstruction of 3-D left ventricular motion from planar tagged cardiac MR images: An estimation theoretic approach. *IEEE Transactions on Medical Imaging 14*, 4 (Dec.), 625 – 635. URL: `ftp://ftp.eng.auburn.edu/pub/tdenney/papers/tmi95.ps.Z`.

DOKOS, S., SMAIL, B. H., YOUNG, A. A., AND LEGRICE, I. J. 2002. Shear properties of passive ventricular myocardium. *American Journal of Physiology 283*, 6 (Dec.), H2650–H2659.

GUTTMAN, M. A., ZERHOUNI, E. A., AND MCVEIGH, E. R. 1997. Analysis of cardiac function from MR images. *IEEE Computer Graphics and Applications 7*, 2 (Feb.), 30 – 38.

HAIRER, E., WANNER, G., AND NØRSETT, S. P. 1993. *Solving Ordinary Differential Equations I - Nonstiff Problems*. Springer Series in Computational Mathematics 8. Springer Verlag.

LAI, W. M., RUBIN, D., AND KREMPL, E. 1986. *Introduction to Continuum Mechanics*, revised edition in SI/metric units ed., vol. 17 of *Pergamon Unified Engineering Series*. Pergamon Press, Headington Hill Hall, Oxford OX3 0BW, England.

LAVIN, Y., LEVY, Y., AND HESSELINK, L. 1997. Singularities in nonuniform tensor fields. In *Proceedings of Visualization '97*, R. Yagel and H. Hagen, Eds., IEEE, 59 – 66.

LEGRICE, I. J., TAKAYAMA, Y., AND COVELL, J. W. 1995. Transverse shear along myocardial cleavage planes provides a mechanism for normal systolic wall thickening. *Circulation Research 77*, 1 (July), 182–193.

LIM, T.-H., AND CHOI, S. I. 1999. MRI of myocardial infarction. *Journal of Magnetic Resonance Imaging 10*, 5 (Nov.), 686 – 693. Special Issue: Cardiovascular MRI.

LORENSEN, W., AND CLINE, H. 1987. Marching cubes: A high resolution 3D surface construction algorithm. *Computer Graphics 21*, 4 (July), 163 – 169. Proceedings of SIGGRAPH '87.

MACKERRAS, P. 1992. A fast parallel marching-cubes implementation on the Fujitsu AP1000. Tech. rep., Department of Computer Science, Australien National University, Aug. URL: `http://cs.anu.edu.au/techreport/1992/TR-CS-10.ps.gz`.

MASOOD, S., YANG, G.-Z., PENNELL, D. J., AND FIRMIN, D. N. 2000. Investigating intrinsic myocardial mechanics - the role of MR tagging, velocity phase mapping and diffusion imaging. *Journal of Magnetic Resonance Imaging 12*, 6 (Dec.), 873–883. URL: `http://www.doc.ic.ac.uk/~gzy/pub/mashood%20tagging%20JMRI%202000.pdf`.

MCCULLOCH, A. D., AND MAZHARI, R. 2001. Regional ventricular mechanics: Integrative computational models of myocardial flow-function relations. *Journal of Nuclear Cardiology 8*, 4 (July), 506–519. Manuscript available at URL: `http://cardiome.ucsd.edu/Publications_files/JNCreview.pdf`.

NIELSON, G. M., AND HAMANN, B. 1991. The asymptotic decider: Resolving the ambiguity in marching cubes. In *Proceedings of Visualization '91*, Computer Society Press, Los Alamitos, California, G. M. Nielson and L. Rosenblum, Eds., IEEE, 83 – 91.

PRESS, W. H., VETTERLING, W. T., TEUKOLSKY, S. A., AND FLANNERY, B. P. 1992. *Numerical Recipes in C - The Art of Scientific Computing*, 2nd ed. Cambridge University Press. URL: `http://www.library.cornell.edu/nr/bookcpdf.html`.

REICHEK, N. 1999. MRI myocardial tagging. *Journal of Magnetic Resonance Imaging 10*, 5 (Nov.), 609 – 616. Special Issue: Cardiovascular MRI.

RUDDY, T. D., DEKAMP, R. A., AND BEANLANDS, R. S. 1999. Taking PET to heart. *eCMAJ - Canadian Medical Association Journal, Electronic Edition 161*, 9 (Nov.), 1131. URL: `http://www.cma.ca/cmaj/vol-161/issue-9/1131.htm`.

SACHSE, F. B., HENRIQUEZ, C., SEEMANN, G., RIEDEL, C., WERNER, C. D., PENLAND, R. C., DAVIS, B., AND HSU, E. 2001. Modeling of fiber orientation in the ventricular myocardium with MR diffusion imaging. In *Proceedings of Computers in Cardiology*, vol. 28, 617–620.

STALLING, D., AND HEGE, H.-C. 1995. Fast and resolution independent line integral convolution. In *Computer Graphics Proceedings (SIGGRAPH '95)*, 249 – 256.

WÜNSCHE, B. C., AND LIN, J. Z. 2003. An efficient and topological correct polygonisation algorithm for finite element data sets. In *Proceedings of IVCNZ '03*, 90 – 95.

WÜNSCHE, B. C., AND YOUNG, A. A. 2003. The visualization and measurement of left ventricular deformation using finite element models. *Journal of Visual Languages and Computing - Special Issue on Biomedical Visualization for Bioinformatics 14*, 4 (Aug.), 299–326.

WÜNSCHE, B. C. 2003. *A Toolkit for the Visualization of Tensor Fields in Biomedical Finite Element Models*. PhD thesis, University of Auckland. (accepted for publication).

WÜNSCHE, B. C. 2003. A toolkit for visualizing biomedical data sets. In *Proceedings of GRAPHITE 2003*, ANZGRAPH and SEAGRAPH, 167–174.

YOUNG, A. A., IMAI, H., CHANG, C.-N., AND AXEL, L. 1994. Two-dimensional left ventricular deformation during systole using magnetic resonance imaging with spatial modulation of magnetization. *Circulation 89*, 2 (Feb.), 740 – 752.

YOUNG, A. A., KRAMER, C. M., FERRARI, V. A., AXEL, L., AND REICHEK, N. 1994. Three-dimensional left ventricular deformation in hypertrophic cardiomyopathy. *Circulation 90*, 2 (Aug.), 854 – 867.

YOUNG, A. A., KRAITCHMAN, D. L., DOUGHERTY, L., AND AXEL, L. 1995. Tracking and finite element analysis of stripe deformation in magnetic resonance tagging. *IEEE Transactions on Medical Imaging 14*, 3 (Sept.), 413 – 421.

YOUNG, A. A., DOKOS, S., POWELL, K. A., STURM, B., MC-CULLOCH, A. D., STARLING, R. C., MCCARTHY, P. M., AND WHITE, R. D. 2000. Regional heterogeneity of function in non-ischemic dilated cardiomyopathy. *Cardiovascular Research 49*, 2 (Feb.), 308–318.